

Supplemental Data

Nuclear Architecture of Rod

Photoreceptor Cells Adapts to Vision

in Mammalian Evolution

Irina Solovei, Moritz Kreysing, Christian Lanctôt, Süleyman Kösem, Leo Peichl, Thomas Cremer, Jochen Guck, Boris Joffe

SUPPLEMENTAL EXPERIMENTAL PROCEDURES

Antibodies

Staining of the nuclear periphery and nucleoli was performed using anti-lamin B (Santa Cruz) and anti-pB23 (Sigma) antibodies, respectively. Nuclear speckles and U2 snRNP were stained using anti-SC35 antibodies (SIGMA) and anti-SF3b66 antibodies ((Will et al., 2002); kindly provided by O.Makarova, University of Leicester, UK). Histone modifications were stained using antibodies directed against trimethylated Lys9 of mouse histone 3 (H3K9me3), trimethylated Lys20 of mouse histone 4 (H4K20me3) (kindly provided by A.H.F.M. Peters, Friedrich Meischer Institute for Biomedical Research, Switzerland), and trimethylated Lys4 of histone 3 (H3K4me3, Abcam). Mitochondria in the inner segment of rod photoreceptors were stained using anti- α subunit ATP-synthase antibodies (Invitrogen). Before immunostaining, sections were air-dried for 30 min and antigen retrieval was performed by heating in 10mM sodium citrate buffer at 80°C for 5min (Yamashita, 2007), unless the retrieval time is specified otherwise.

Probes for DNA and RNA FISH

Probes against mouse repeat sequences were generated by PCR using the following primers:

major satellite 5'-GCGAGAAACTGAAAATCAC and 5'-TCAAGTCGTCAAGTGGATG;

minor satellite 5'-ATATGTGCGACTGAAAAACACATTCGGTTGG

and 5'-ATATACTAGTGTGGTTTTTCATCATCATTTTC (Pietras et al., 1983);

LINE1 5'-GCCTCAGAACTGAACAAAGA and 5'-GCTCATAATGTTGTTCCACCT;

B1 5'-CACGCCTGTAATCCCAGC and 5'-AGACAGGGTTTCTCTGTA;

telomeres 5'-(TTAGGG)₅ and 5'-(CTTACC)₅ (Ijdo et al., 1991; Kipling and Cooke, 1990).

In all cases, mouse genomic DNA was used as a template and hapten- or fluorophore-conjugated dUTP was included in the reaction.

The following BAC clones were purchased from the BACPAC Resources Center (<http://bacpac.chori.org>):

RP23-95B6 (comprising the β -actin gene, *Actb*), RP24-288E4 (α -tubulin, *Tuba1*), RP24-363O8 (nucleophosmin, *Npm1*), RP23-326O5 (lysozyme, *Lyzs*), RP23-266J21 (hemoglobin alpha adult chain 1, *Hba-a1*), RP24-86N10 (keratin, *Krt1-1*), RP23-214J2 (GLAST, *Slc1a3*), RP23-219M6 (rod opsin, *Rho*), RP23-241A8 (rod outer segment membrane protein 1, *Rom1*), RP23-53N22 (phosducin, *Pdc*), RP23-61I21 (retinitis pigmentosa 1 homolog, *Rp1h*). BAC probes were labeled by nick-translation using biotin, digoxigenin, Cy3, TAMRA or fluorescein that had been conjugated to dUTPs according to (Henegariu et al., 2000).

Probes were dissolved in hybridization mixture (50% formamide, 10% dextran sulfate, 1xSSC) at a concentration of 10-20ng/ μ l in the case of repeated sequences and at concentration of 50-100ng/ μ l for BAC DNA and chromosome paints.

For RNA FISH, a 50mer oligonucleotide (CCCTGCCXAATTCCCAAGCAGTCACXAACAAGC

AGAGACCATXAGGATGG, where X is amino-C6-dT) complementary to nt 1882-1931 of mouse rhodopsin (GenBank NM_145383) was conjugated to the Cy3 fluorophore using its NHS ester derivative (GE Healthcare Life Sciences). Labeled oligos were purified by gel filtration chromatography on Sephadex G50 fine.

Microscopy and image analysis

Image stacks were corrected for chromatic shift as described by Walter et al. (2006). The analysis of the radial distribution along the relative radius was on performed using the RRD program (Cremer et al., 2001); the analysis of distances from the nuclear border was carried out using the ADS program (Albietz et al., 2006). Statistical analysis of these data was performed as described by Ronneberger et al. (2008) using SigmaStat software (Systat Software Inc.).

Quantification of photoreceptor areal density

Photoreceptor density data for fallow deer, horse and chipmunk were not available in the literature and were obtained for this article by L.Peichl. Briefly, whole retinae or retinal pieces were immunolabelled for cone opsins, using peroxidase-antiperoxidase/diaminobenzidine visualization (Peichl et al., 2000). The retinae were flatmounted photoreceptor side up, cones were counted in 250 μm x 250 μm sample fields with a x40 or x63 objective, and the counts were converted to cells/ mm^2 . In the same preparations, total photoreceptor densities were counted in digital micrographs taken with differential interference contrast optics and a x100 objective, and rod densities were derived by subtracting cone density from total photoreceptor density. Data for other species were taken from (Dkhissi-Benyahya et al., 2001; Gerke et al., 1995; Hallett, 1987; Jeffery et al., 1994; Jeon et al., 1998; Krebs and Friedrich, 1982; Peichl et al., 2000; Steinberg et al., 1973; Szel and Rohlich, 1992; Wikler et al., 1990; Young and Vaney, 1990).

FDTD Simulations

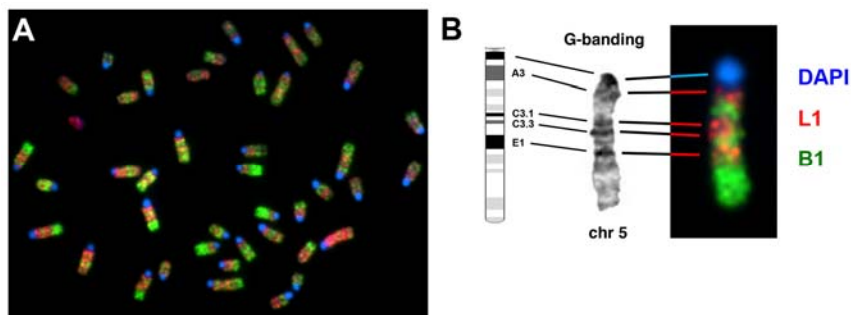
We have simulated the passage of light through single nuclei using a 2D finite-difference time-domain (FDTD) algorithm ("Meep FDTD package," <http://jdj.mit.edu/meep>; see also (Farjadpour et al., 2006). Based on TEM data and original DNA staining for mouse rod nuclei we infer a difference in DNA density between the central heterochromatin mass and euchromatin, which can safely be assumed to translate into differences in refractive index inside of the nucleus. This is in agreement with the qualitative phase contrast observations and the quantitative phase profile measurements. Given that refractive index scales linearly with molecular density (Barer, 1954) and that the average refractive index of nuclei is in the range of 1.38–1.41 (Brunsting and Mullaney, 1974; Drezek et al., 1999), we used refractive indices of 1.385 and 1.415 for the euchromatin and heterochromatin regions, respectively. The refractive index of the surrounding tissue was taken to be 1.360, which is in accordance with values measured for single bipolar cells in the retina as well as earlier estimates for the total retina (Franze et al., 2007). Variations in refractive index of up to ± 0.02 around the average within single nuclei in response to changes of chromatin amount and/or arrangement have been reported before (Drezek et al., 2003). The assumed refractive index difference of the two chromatin phases of 0.03 falls into this range and is in good agreement with quantitative phase images.

Optical properties of the two nuclear patterns were studied both by looking at the scattering of a plane wave by single nuclei and the propagation of a spatially confined wave through a ten nuclei thick ONL with hexagonal structure. For the latter, lattice points were randomly displaced by a small amount to better resemble the situation in vivo. The wavelength of light was generally set to 500 nm to match the peak sensitivity of the rod photoreceptors (Lyubarsky et al., 1999). The factitious rectangular geometry of the light source for ONL simulations was chosen because it includes a broad spectrum of transverse frequencies, which helps avoiding an accidental resonance of the system.

Quantitative phase measurements

Mouse retina was excised from eyes immediately after animals were sacrificed; pig eyes were stored on ice for not more than 1.5-2 h as necessary to deliver them to the laboratory. To isolate rod cells, retina was incubated in PBS with papain (0.15 μ l/ml) and DNase (0.1 μ l/ml) for 10-15 min at 37°, then pieces of retina were transferred to PBS and disintegrated by gentle pipetting. For phase retardation measurements, a drop of cell suspension in PBS was placed on a microscopic slide and covered with a cover slip. The presence in suspension of larger tissue fragments assured that isolated nuclei around them were not flattened. Images were recorded on a compensated Jamin-Lebedev interferometric microscope (Zeiss) using a 40x objective (NA 0.65), a monochromatic light source (546 nm, FWHM 5 nm) and a calibrated CMOS camera. For the calibration of the microscope both a linearly phase-shifting wedge and micron-sized droplets of known refractive index were used. The visibility of interference fringes from test samples was measured to be > 98%. Raw interferograms (Figure 8A) were converted into actual quantitative phase maps (Figure 8B) by demodulation of the measured pixel values with the inverse transfer function of the microscope using Matlab.

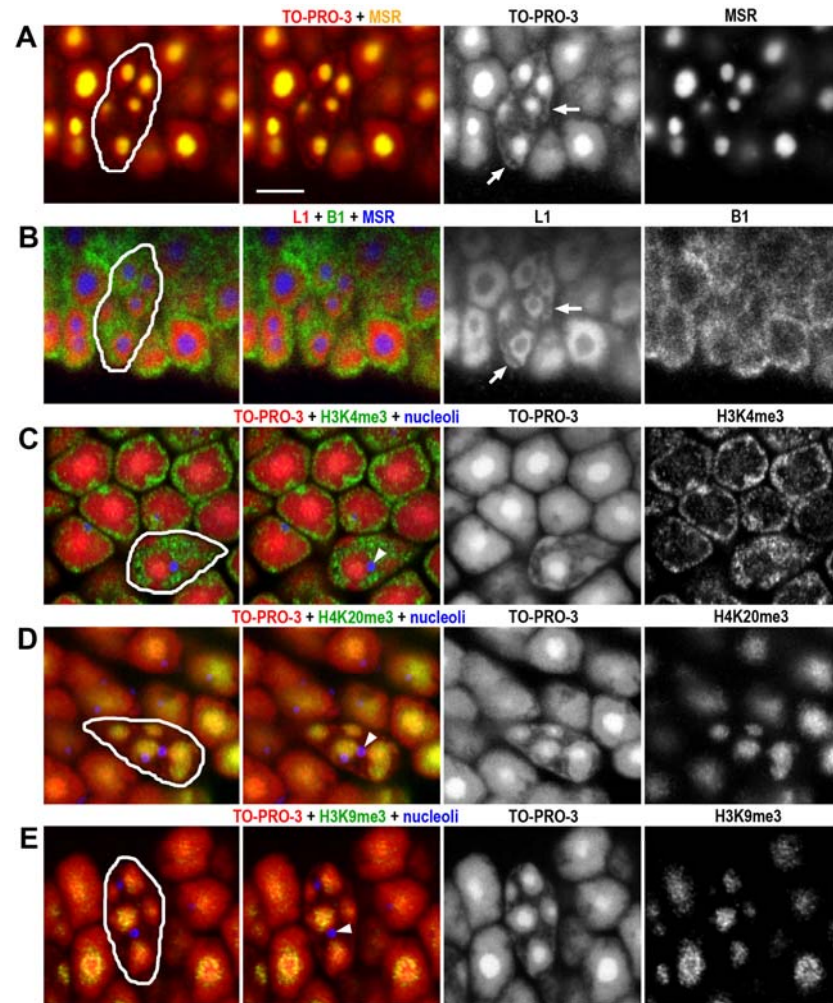
Figure S1. Banding pattern of mouse mitotic chromosomes after FISH with probes for marker chromatin sequences



(A) Metaphase spread from a mouse embryonic stem cell (43,XY) shows a banding pattern corresponding to G- and R-bands. FISH was performed with probes for L1 (red, L1-rich heterochromatin) and B1 (green, euchromatin), DNA was counterstained with DAPI (blue) that strongly stains pericentromeric heterochromatin.

(B) Correspondence of the conventional G-banding and hybridization pattern of the two probes exemplified for MMU5 (identity of MMU5 was confirmed by FISH with the respective chromosome paint, not shown). Ideogram of chromosome 5: Ensemble database; G-banding image: D.Chapman, courtesy of the Department of Pathology, University of Washington, USA.

Figure S2. Nuclear architecture of mouse cone cells.

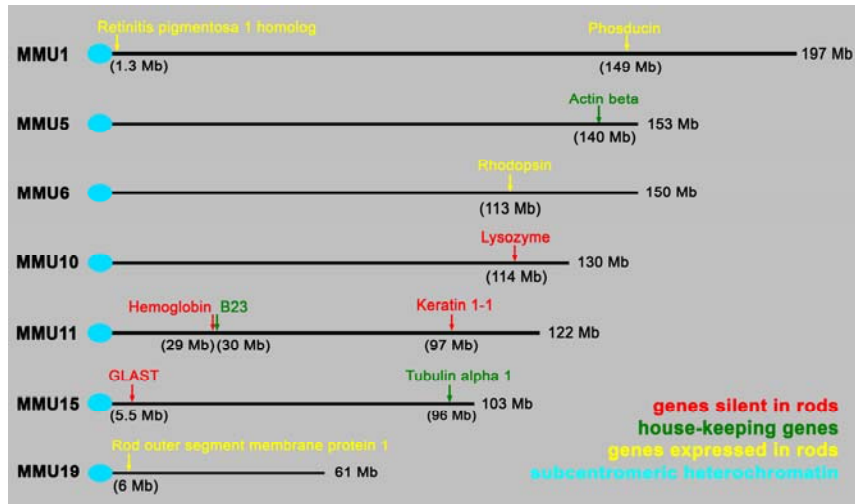


Mouse cones have the conventional nuclear architecture, readily discernible from that of the rods. In mouse, cones are rare (3%); single cone nuclei (outlined in the left column) are usually situated at the outer margin of the ONL, surrounded by rod nuclei.

(A,B) Distribution of marker DNA sequences; A and B show the same cone cell. (A) Cone nuclei possess several chromocenters revealed by FISH with MSR probe (yellow in overlay); each chromocenter is surrounded by heterochromatin less brightly labeled by the nuclear counterstain TO-PRO-3 (red in overlay), while large (euchromatin) regions in cone nuclei are only very weakly stained with TO-PRO-3. A thin rim of heterochromatin aligns the borders of cone nuclei (TO-PRO staining, arrows). (B) The material surrounding chromocenters (MSR, blue) is L1-rich chromatin (red) which also forms a rim along the nuclear border (arrowheads).

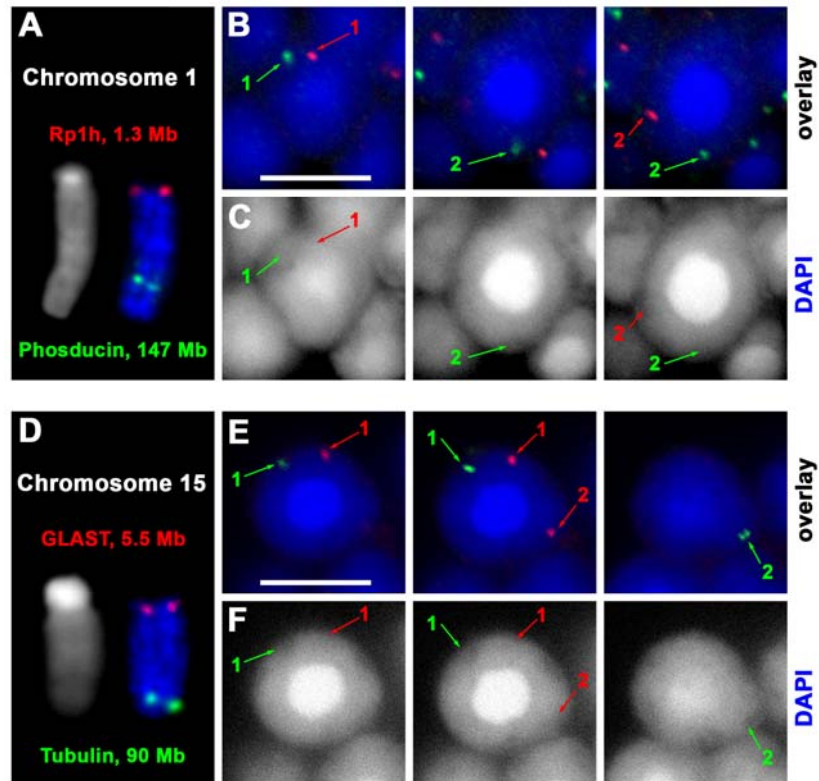
(C-E) Immunostaining for marker histone modifications (green) and nucleoli (blue, arrows) corresponds to the distribution of marker DNA sequences. (C) H3K4me3, characteristic for euchromatin, is observed in the inner portions of the cone nucleus. In difference to rods, the nucleoli have an inner position (arrows). (D) H4K20me3 (after 30 min antigen retrieval) labels chromocenters and heterochromatin surrounding them. (E) H3K9me3 labels only chromocenters. Single confocal sections. Scale bar: 5 μ m.

Figure S3. Chromosomal positions of genes used in this study



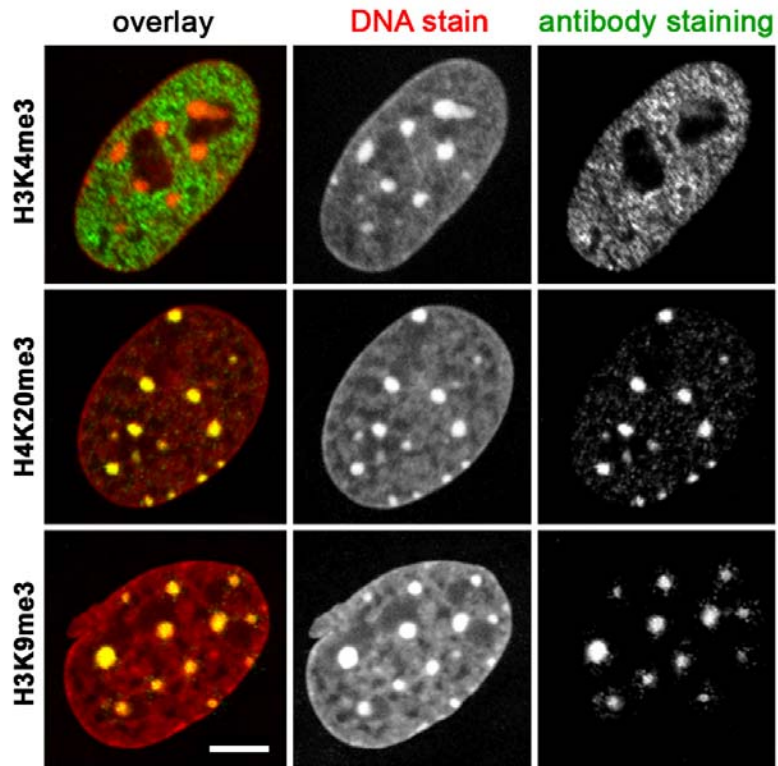
The black lines represent chromosomes. Numbers at the right indicate the DNA content (Mb). The numbers in parentheses show genomic distances from genes to subcentromeric heterochromatin according to ENSEMBLE database.

Figure S4. Nuclear positions in rod cells of genes located in chromosomes close to the subcentromeric heterochromatin



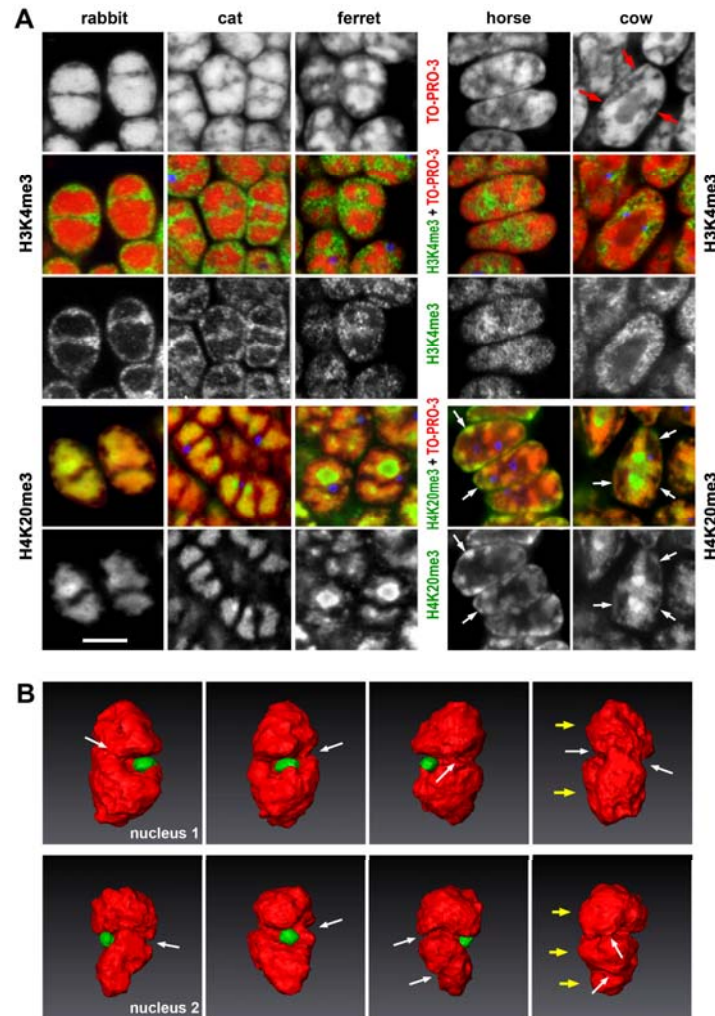
Genes positioned next to the subcentromeric heterochromatin in mitotic chromosomes localize at the periphery of rod nuclei during interphase – just as all other genes – and are therefore widely separated from the centrally located chromocenter. We visualized the nuclear positions of 2 such genes (red); for comparison, nuclear positions of genes with distal location on the same chromosomes (green) were also visualized. The positions of signals in relation to the nuclear border are indicated by arrows. (A-C) MMU1: retinitis pigmentosa 1 homolog gene (*Rp1h*, red) and phosducin gene (*Pdc*, green). (D-F) MMU15: GLAST gene (*Slc1a3*, red) and α -tubulin gene (*Tuba1*, green). (B,C,E,F) Three confocal sections through each nucleus are shown to demonstrate the positions of both homologues (1 and 2) of each gene. Scale bars: 5 μ m.

Figure S5. Spatial distribution of histone modifications in nuclei of mouse embryonic fibroblasts



H3K4me3 (green), a marker of euchromatin, occupies most of the nucleus, but is absent at the peripheral nuclear rim (red in overlay with TO-PRO-3 counterstain). Both markers of heterochromatin, H4K20me3 and H3K9me3 (yellow in overlay with TO-PRO-3 counterstain) label chromocenters (c.f. Schotta et al., 2004). Confocal mid sections. Scale bar: 5 μ m.

Figure S6. Nuclear architecture of rod cells in five mammalian species



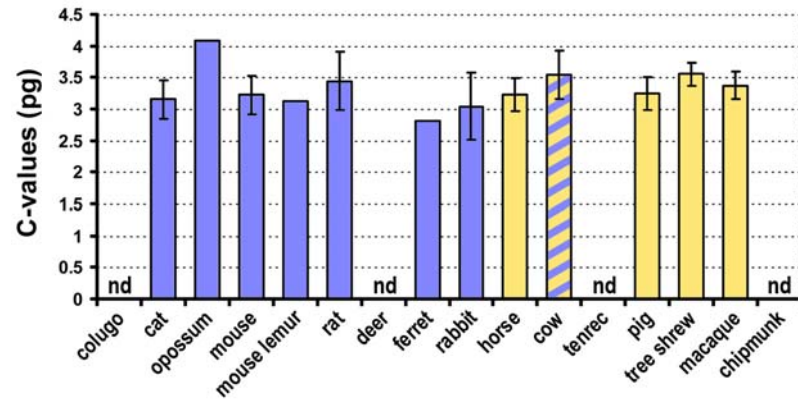
(A) Distribution of euchromatin (H3K4me3) and heterochromatin (H4K20me3 after 30 min antigen retrieval) in rod nuclei of 5 species not presented in Fig 5. In overlays, histone modifications are shown in green, DNA counterstain with TO-PRO-3 in red, nucleoli (anti-pB23) in blue. Single confocal sections. Scale bar: 5 μ m.

(B) Amira 3D reconstructions of the central heterochromatin mass (H4K20me3, red) of two rod nuclei from cat. Each row shows one nucleus from different view points. Some of the clefts in the heterochromatin mass are indicated by white arrows. Note a bipartite shape of the nucleus 1 and a tripartite shape of the nucleus 2. The single nucleolus (green) takes a position in a concavity of the heterochromatin mass.

Rabbit, cat and ferret have elongated rod nuclei with the inverted pattern. Observed in optical sections, the heterochromatin mass appears to be separated to 2-3 regions. 3D reconstructions, however, confirm their connection into a single central heterochromatin mass (exemplified for cat, B). Its complex shape suggests an incomplete fusion of heterochromatin clusters (compared to the complete fusion into a single compact central heterochromatin mass in mouse rod nuclei, Fig. 4). Some euchromatin (H3K4me3) can expand into the nuclear interior along invaginations of the heterochromatin mass.

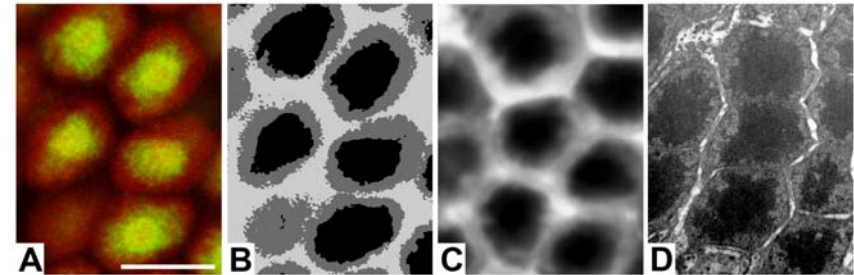
Horse rod nuclei have a typical conventional pattern, whereas bovine rod nuclear architecture shows an intermediate character. On one hand, the clearly manifested rim of heterochromatin at the nuclear border (red arrows) is typical for the conventional pattern; on the other hand, these nuclei contain a single chromocenter located in the central part. Note that other retinal characteristics are also intermediate in cow (see Fig 6).

Figure S7. Genome size of the studied species



Despite different rod nuclear volumes (c.f. Fig 5E), the species with the inverted, intermediate and conventional rod nuclear pattern have similar C-values (blue, striped and yellow columns, respectively). The values shown are means of the estimates included in the genome size database (Gregory et al., 2007); bars show minimal and maximal values. Nuclear volume and DNA content do not correlate (both Pearson correlation coefficient and Spearman rank correlation coefficients were low and not significant). nd, not determined.

Figure S8. Eu- and heterochromatin compartments in mouse rod nuclei: comparison of three visualization methods

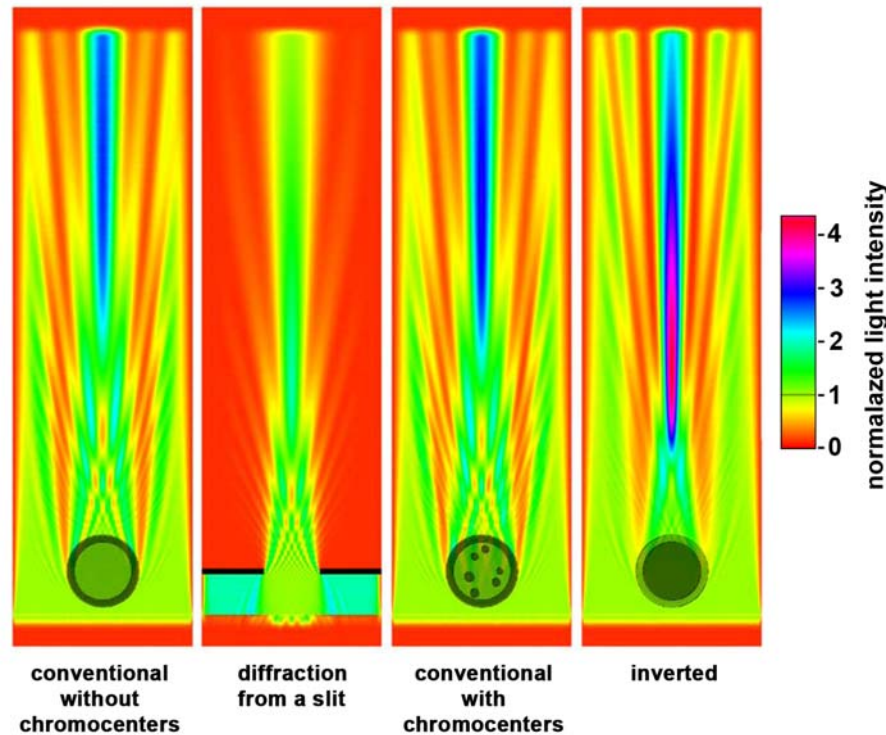


Antibody staining of heterochromatin and TEM observations show that the region of increased refractive index in rod nuclei corresponds to the central heterochromatin mass.

(A) Original image of rod nuclei after anti-H4K20me3 staining (green) and nuclear counterstain with TO-PRO-3 (red); confocal optical section. (B) The same image after segmentation. (C) Rod nuclei imaged *in vivo* using phase-contrast. (D) Transmission electron-microscopic image (courtesy S.Haverkamp, MPI for Brain Research). Scale bar: 5 μ m

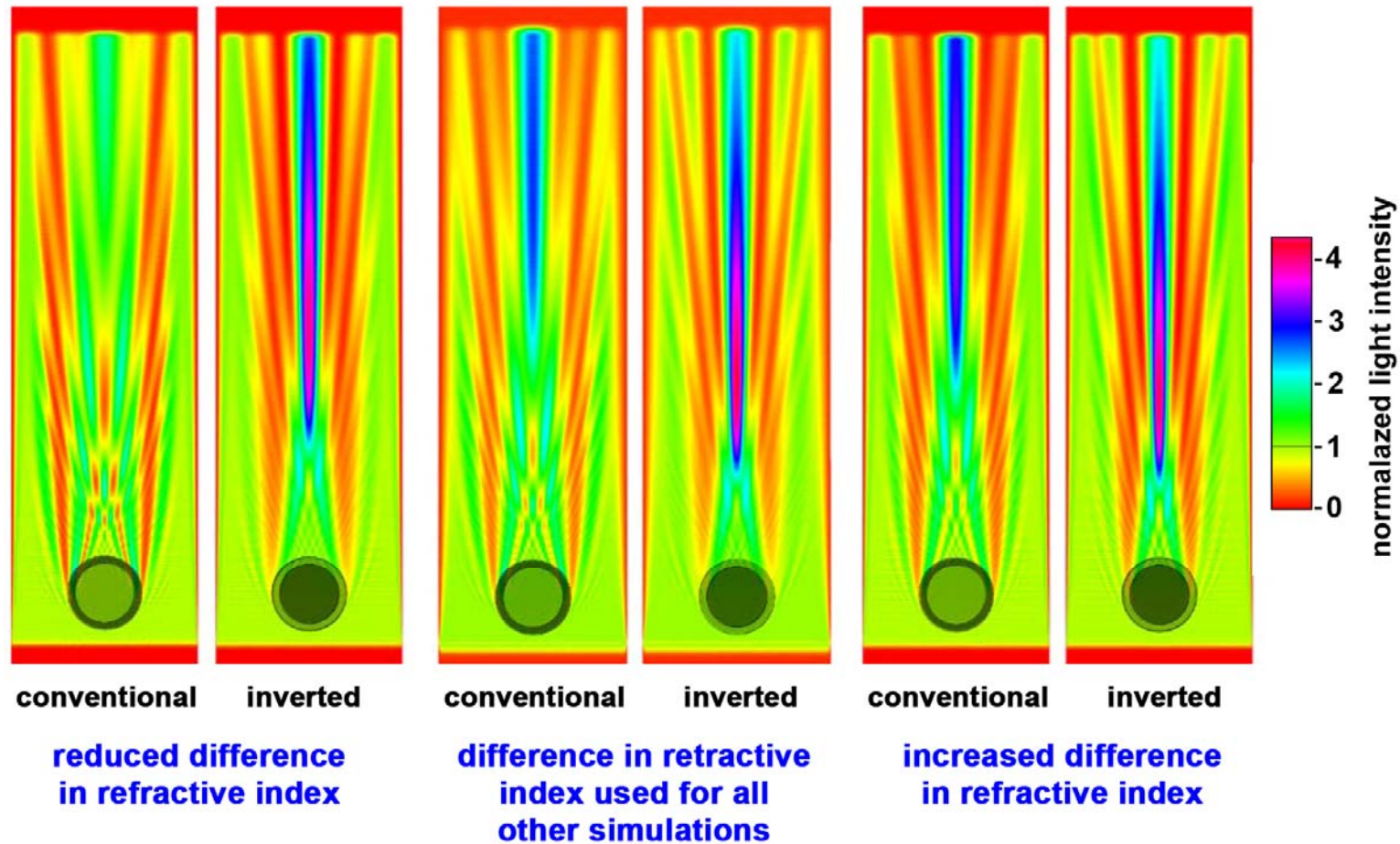
Figure S9. Parameter variations for simulations of single nucleus

(A) Analysis of plane wave scattering by nuclei of different architecture



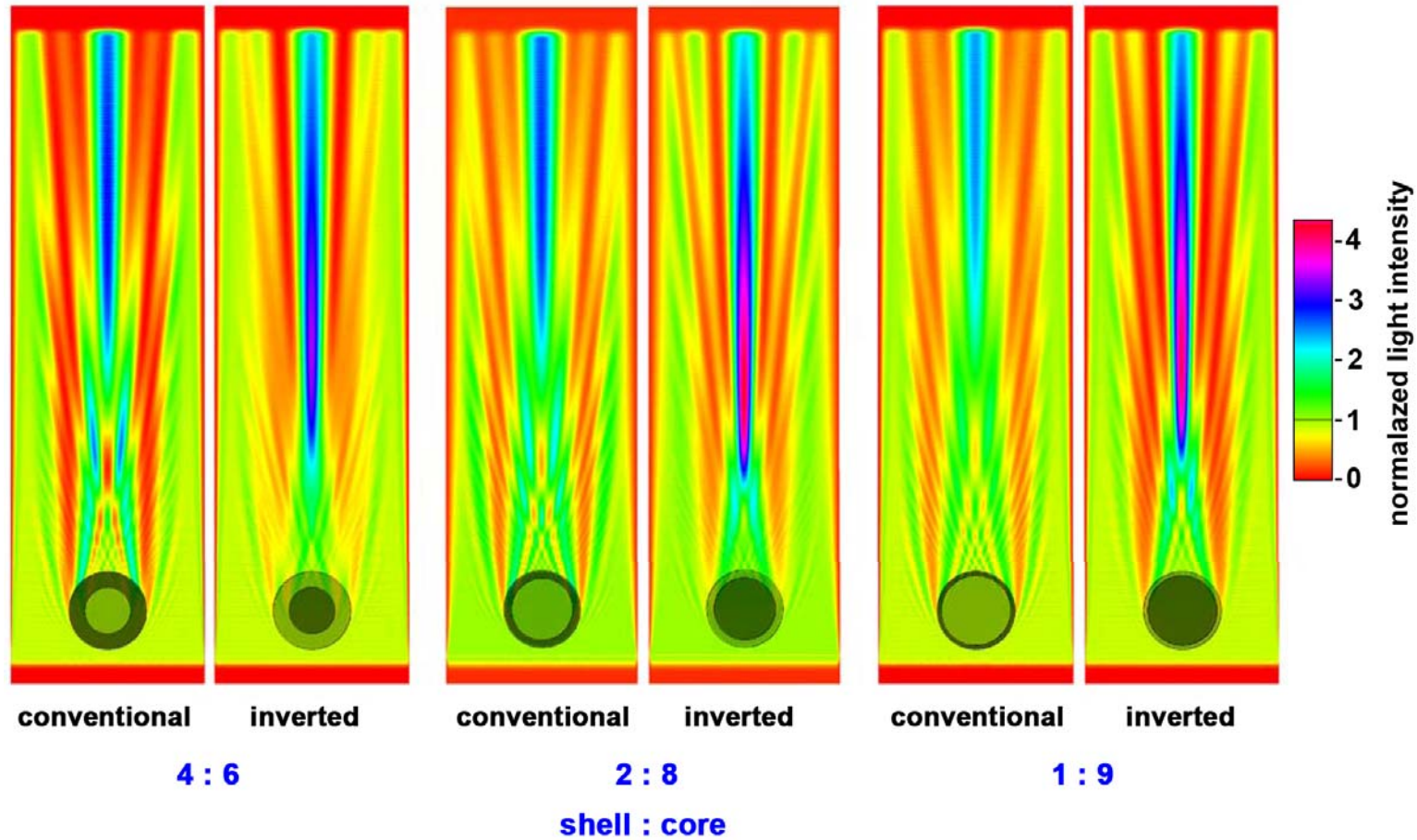
The refractive indices of the medium, euchromatin and heterochromatin are 1.36, 1.385, and 1.415, respectively. The diameter of the nuclei is $5\ \mu\text{m}$, corresponding to 10 wavelengths at the wavelength of 500 nm. The ratio of inner to outer diameter is 0.8. These values also serve, unless indicated differently, as fixed basis for the following parameter variations. In all figures, euchromatin is shown with a lighter shade of green than heterochromatin. The linear color scale shows the color code for intensity of the light field normalized to the incident intensity. A comparison of the conventional nucleus (without chromocenters) to the near field diffraction pattern from a slit of same size shows that the scattering signal from a conventional nucleus is dominated by diffraction. Adding chromocenters (refractive index 1.415 as for all heterochromatin) to the conventional nucleus does not change the scattering pattern significantly. In contrast to the conventional nucleus, the nucleus with the inverted pattern (heterochromatin in the center and euchromatin in the shell) shows a strong focusing behavior: note a zone of high intensity behind the inverted nucleus.

(B) Refractive index variations



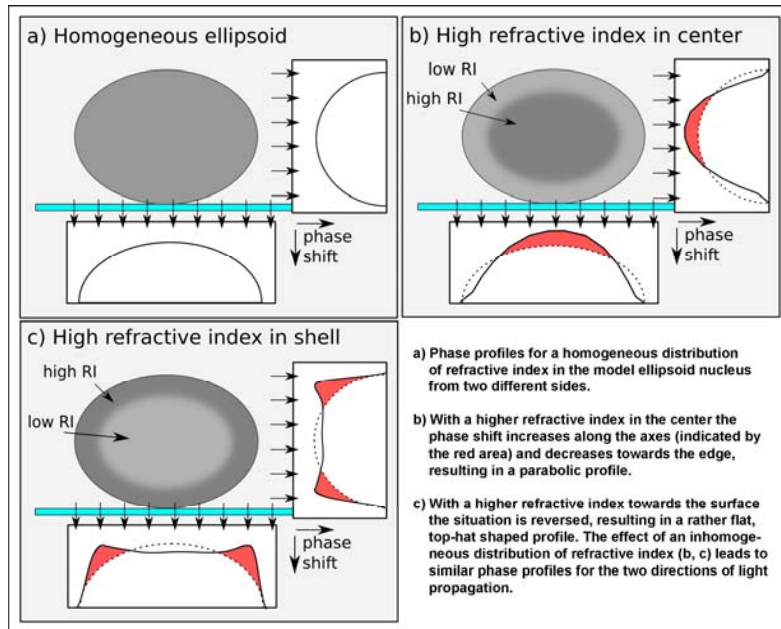
The scattering pattern behind nuclei of the conventional architecture shows increasing similarity to the diffraction pattern of a slit (see A) when the difference between the refractive indices of eu- and heterochromatin decreases. Increasing the refractive index difference in the case of the inverted nucleus lowers the focal length, as one would expect. Refractive indexes for eu- and heterochromatin are 1.395 and 1.41 (left), 1.385, and 1.415 (center), 1.37 and 1.42 (right), medium 1.36.

(C) Variation of relative width of the heterochromatic core and euchromatic shell



The refractive power of the inverted nucleus increases with increasing core size, whereas it decreases for the conventional architecture, both as would be expected. Variations of the relative size of the core do not have a large impact on the optical consequences of the inverted pattern, unless the core becomes too small. Indeed, as illustrated in the main text and Supplemental Table S2, in the rods of nocturnal species the euchromatin shell is always narrow.

Figure S10. Schematic of the dependence of phase profiles on the distribution of refractive index in an egg-shaped model nucleus laying on a microscope slide (blue rectangle)



Mouse rod nuclei, although spherical, have phase shift profiles of the type shown in (b), while phase shift profiles of pig rods are of the type shown in (c). A predominantly central location of the material with a higher refractive index (b) leads to similar phase profiles for light propagating perpendicularly or parallel to the surface of the slide. The same is true for a predominantly peripheral location (c). Hence, our measurements enable us to make reliable conclusions also for light propagating along the long axis of the elongated rod nuclei as it takes place in pig retina.

Figure S11. Representative examples of phase shift profiles for the cells types studied

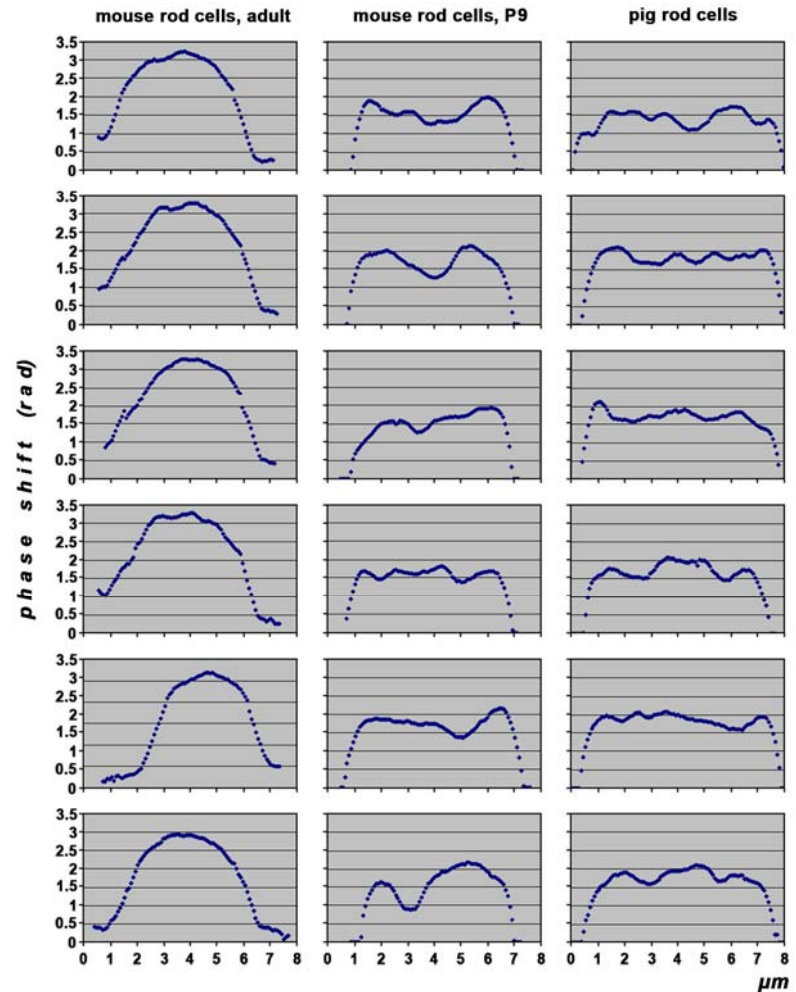
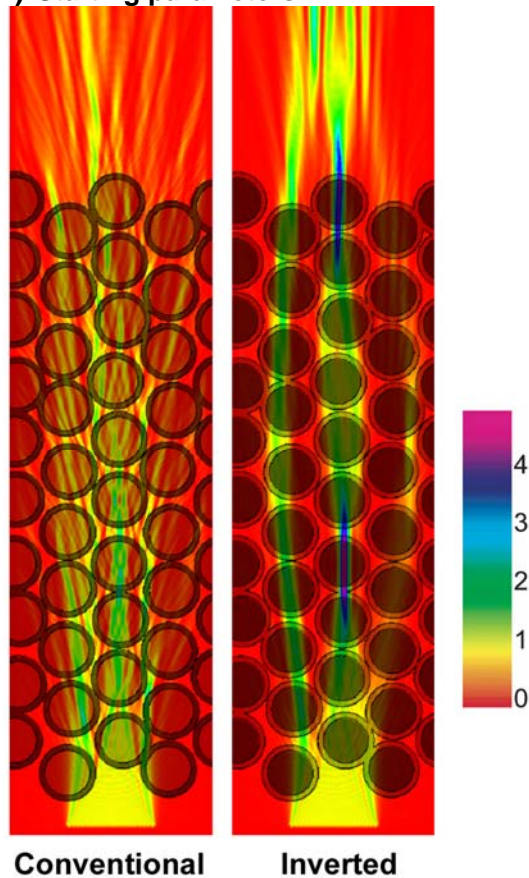


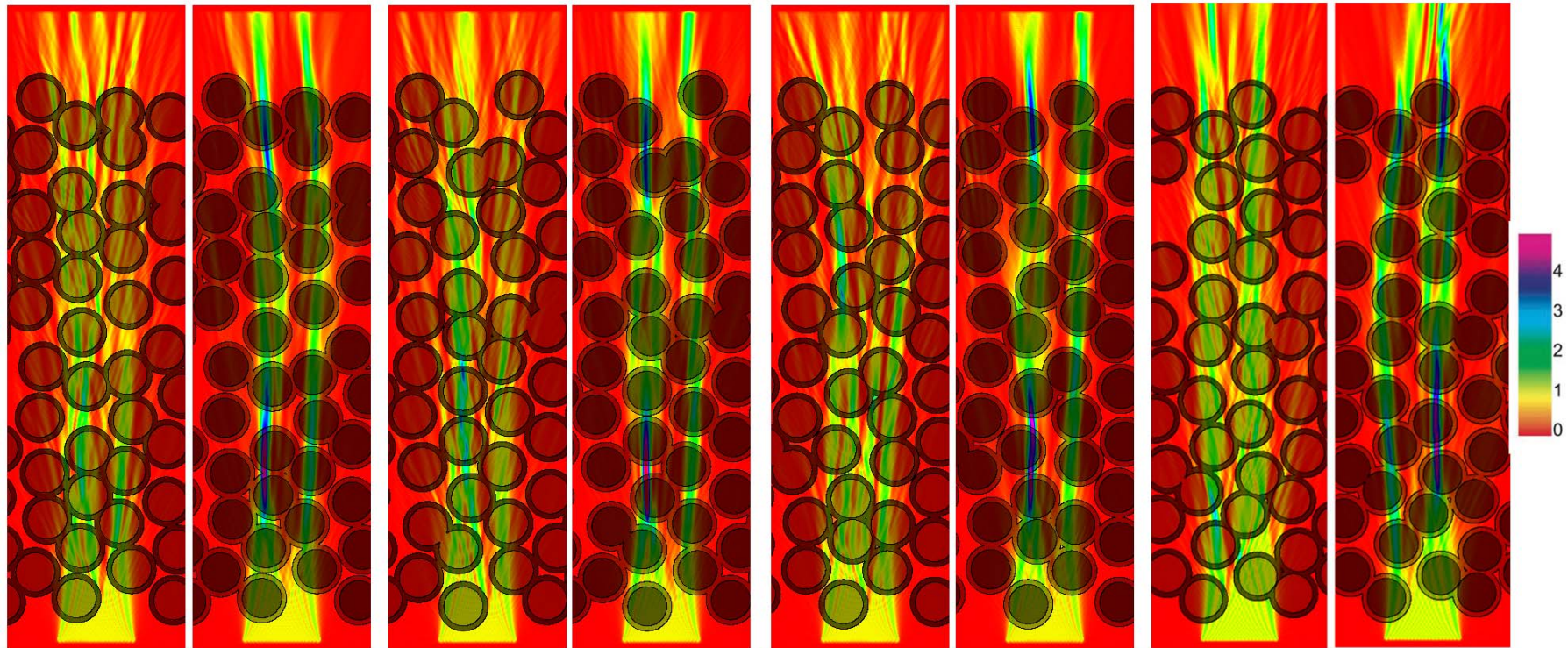
Figure S12. Parameter variations for simulations of the ONL

(A) Starting parameters



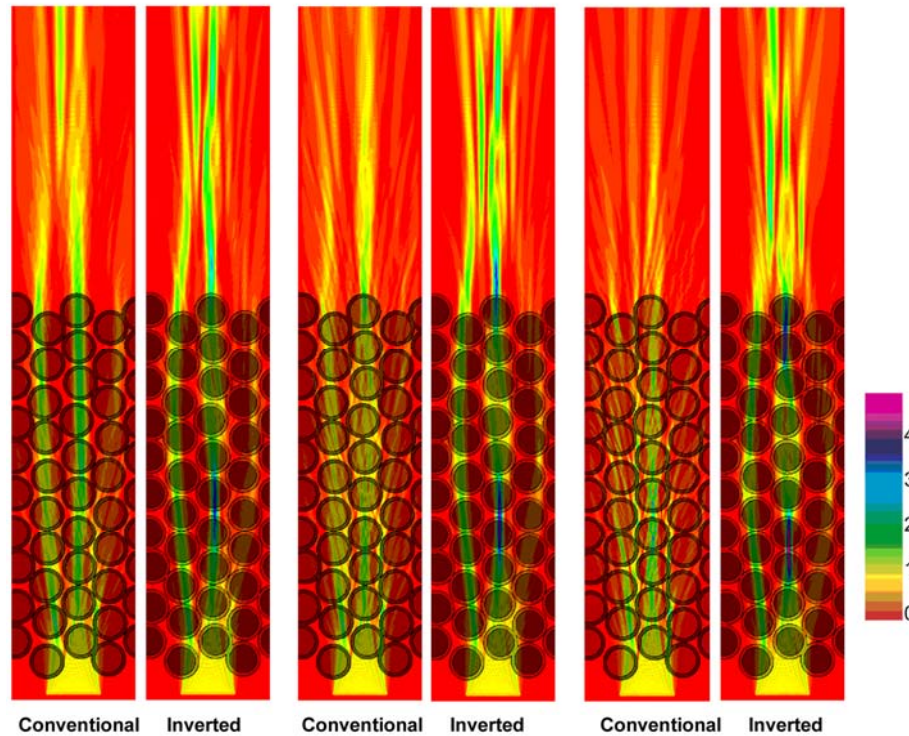
Original simulations have been performed on an outer nuclear layer (ONL) model consisting of columns of 10 nuclei arranged in a hexagonal lattice with a small noise term. Parameters for the individual nuclei were the same as indicated in the legend to Figure S9A. For illumination, a confined plane wave was chosen to avoid an accidental match with an eigenfunction of the optical system. The inverted nuclear architecture results in focusing of incident light and an improved transmission of light through the ONL with much reduced scatter.

(B) Variations of the random displacement (regularity of columns)



Images show light transmission in four different specific ONL arrangements obtained by random displacement of rod nuclei. The four ONL arrangements present three runs of an identical algorithm displacing the centers of nuclei in random directions and with random amplitudes away from an exact hexagonal lattice. The resulting displacements are even bigger than those observed in native retina. Each pair of images shows the results obtained with identically arranged conventional (left) and inverted (right) nuclei. As can be seen, even in the case of big lattice distortions the inverted nuclei still maintain light transmission with much reduced scatter and light staying confined to the “original” columns. This simulation illustrates that the improved light transmission by nuclei with the inverted pattern is very robust against the degree of the irregularity of columns. Note that in native retinas rod perikarya are always packed densely. Thus, one can rather expect light escaping to a neighboring column than strong scattering due to irregularities in the lattice of inverted nuclei.

(C) Refractive index variations

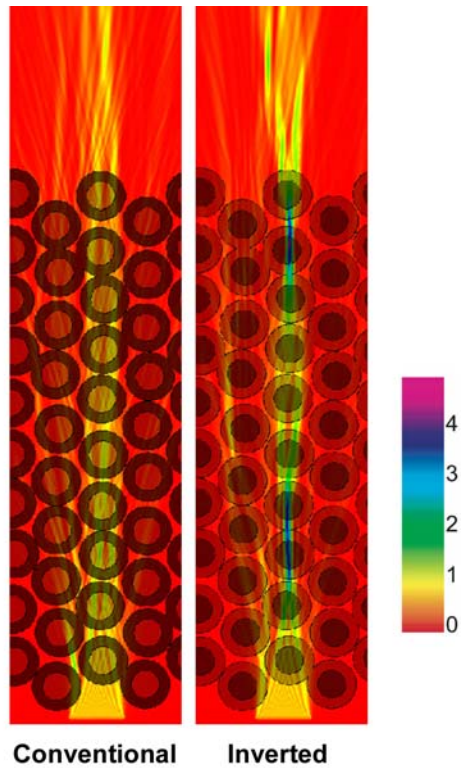


Refractive index value for the medium in all cases is 1.36. Refractive indexes for eu- and heterochromatin are 1.39 and 1.41 (left), 1.40 and 1.41 (center), 1.38 and 1.42 (right). Results of our simulations were found to behave physically reasonable under variations of refractive indices. Towards the limit of small refractive index differences between hetero- and euchromatin, the solutions for the conventional and the inverted ONL become more and more similar (even though improved transmission can still be observed for refractive index differences as small as 0.01). An improved light transmission with reduced scatter is observed in the case of inverted nuclei irrespective of the refractive index difference chosen.

Refractive indexes values for eu- and heterochromatic domains

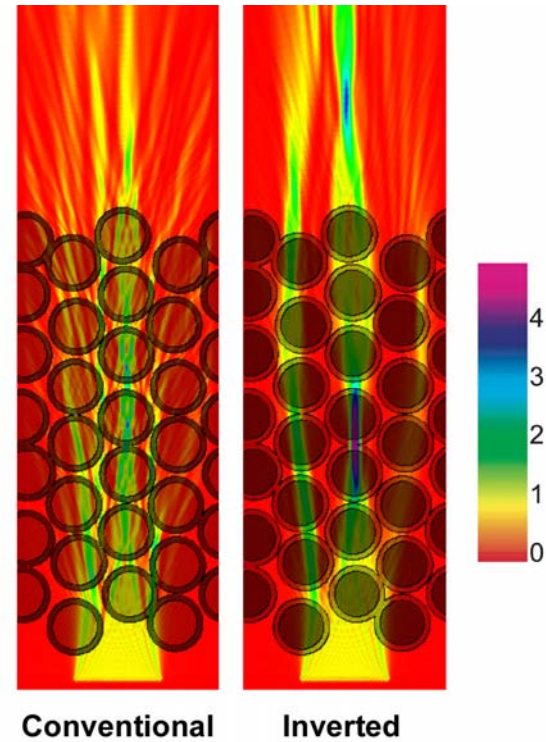
1.40	1.39	1.38
1.41	1.41	1.42

(D) Variations of nuclear size



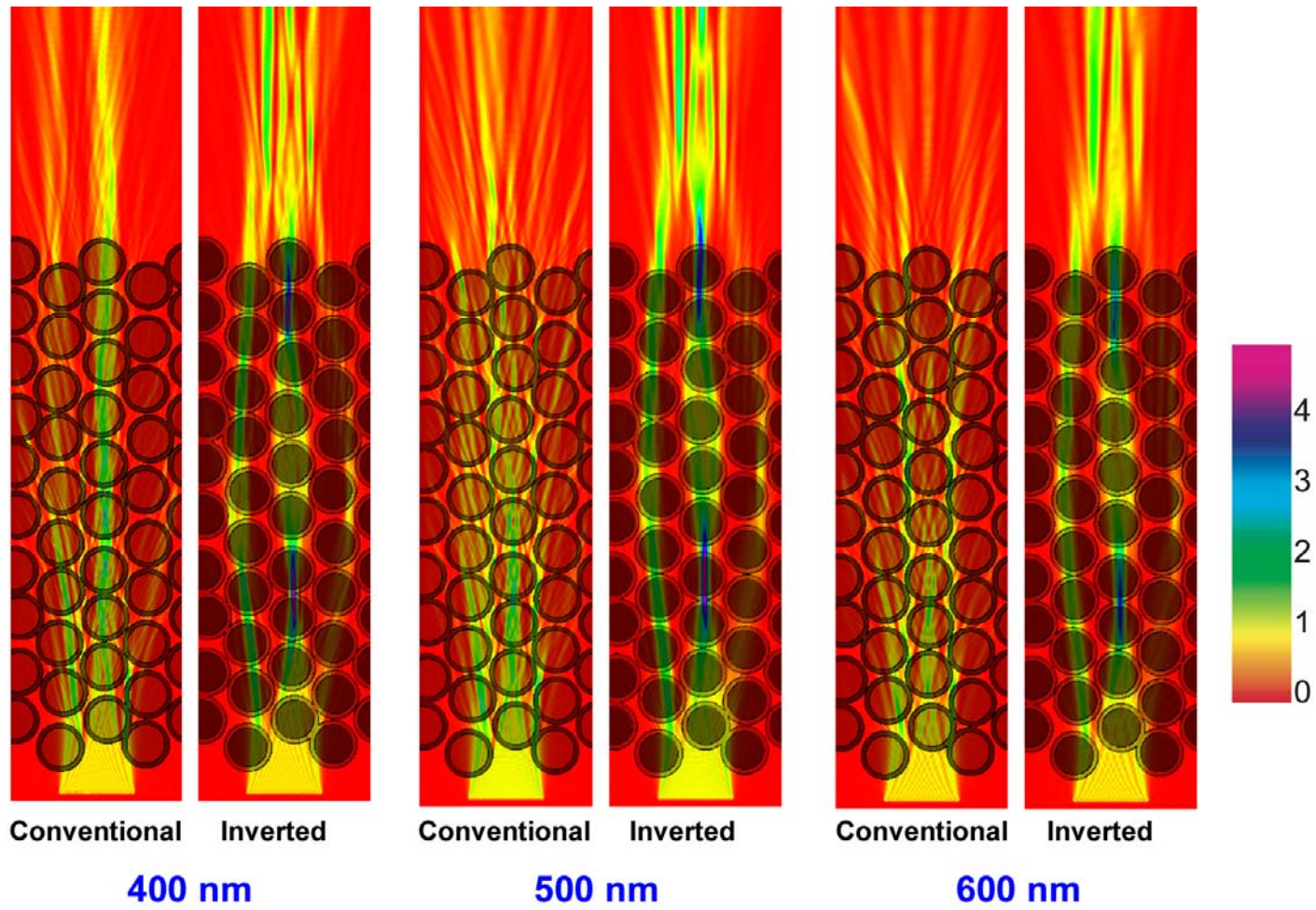
We checked our model to be robust against variations in absolute nuclear size. Shown here: ONL with nuclei of increased outer diameter (7 μ m). All other parameters are unchanged.

(E) Variations in number of ONL tiers



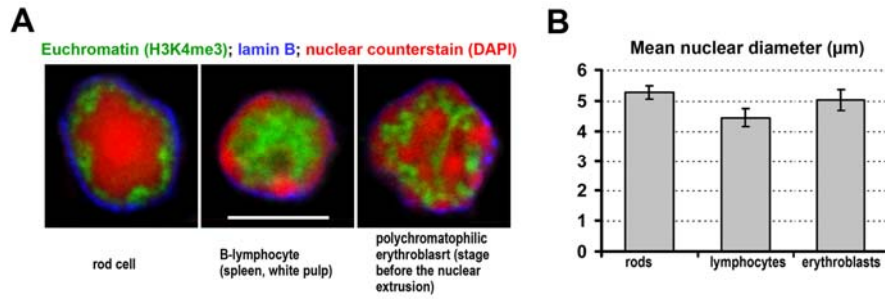
The improved light transmission with much reduced scatter in case of the inverted architecture was found to be robust against variations of ONL thickness. Here: reduced thickness of 7 tiers. The results look similar to those for 10 tiers.

(F) Variations in wavelength



Improvement of light transmission through ONL due to the inverted pattern is robust against changes of wavelength.

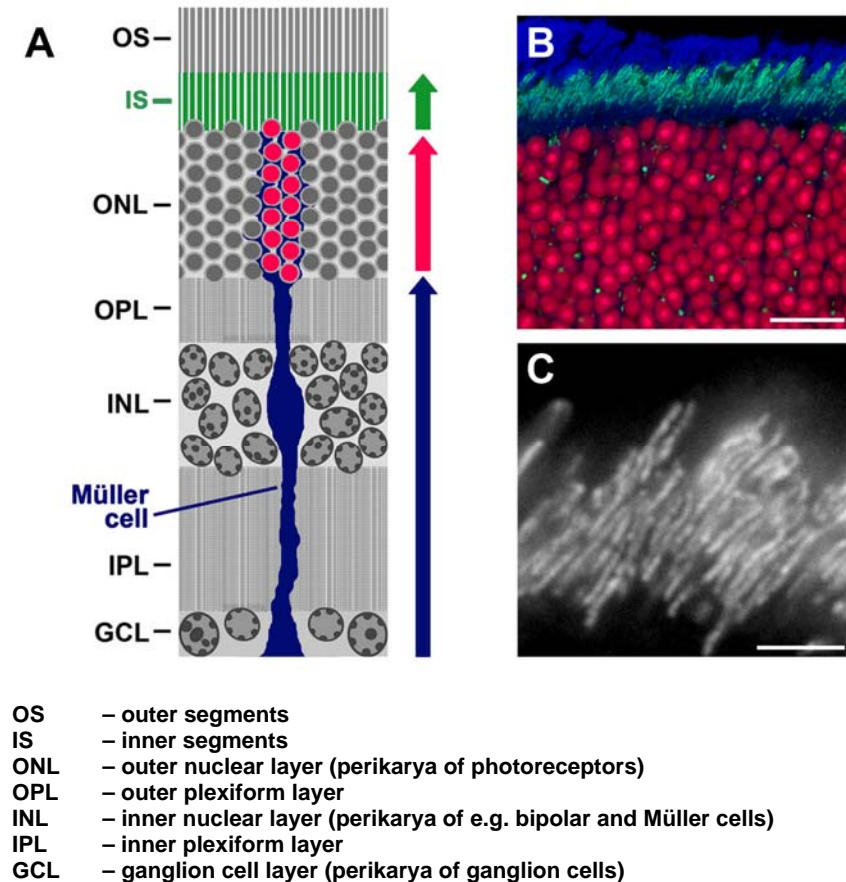
Figure S13. The distribution of euchromatin and heterochromatin in three cell types with small nuclei



(A) The distribution of euchromatin (anti-H3K4me3 immunostaining, green) and heterochromatin (DAPI counterstain, red) in the nuclei of three mouse cell types characterized by the smallest nuclear size. Nuclear envelope is visualized by anti-lamin B2 immunostaining (blue). For clarity, surrounding nuclei were deleted from images. Scale bar: 5 μm . For description of erythropoiesis at TEM level see Djaldetti et al. (1972).

(B) Mean sizes of nuclei of the cell types shown in A. Error bars: 95% confidence intervals.

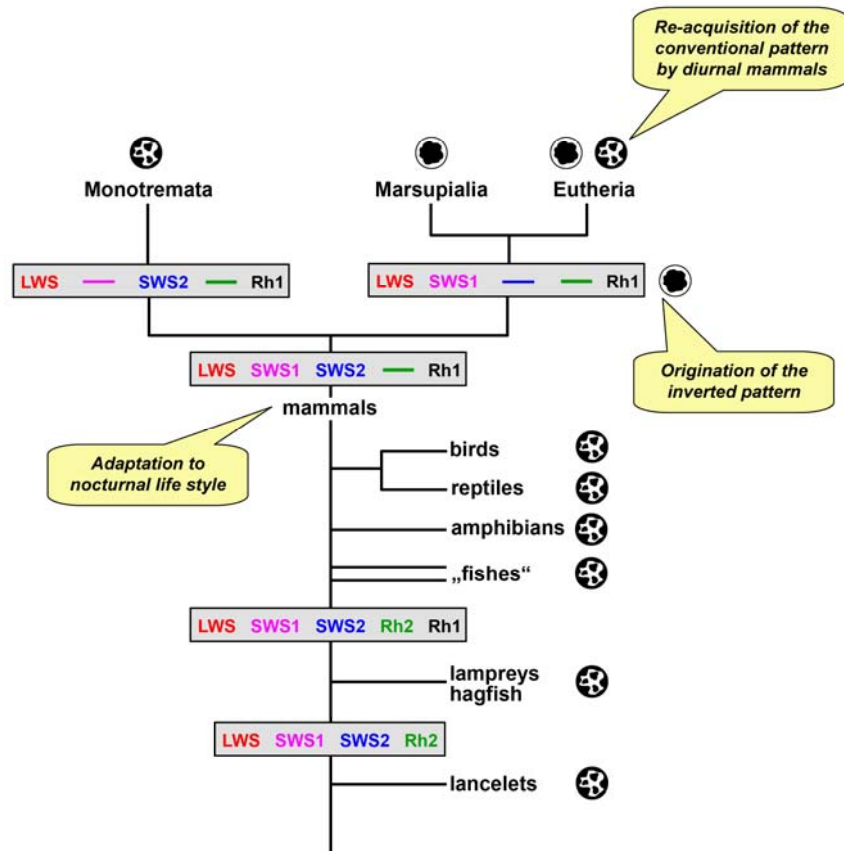
Figure S14.



(A) Putative scheme of light guiding through the nocturnal retina. (B,C) Mitochondria visualized in the inner segment layer. Mitochondria (green in B) were labeled using antibodies to α -subunit of ATP-synthase. Only a few mitochondria adjoin rod nuclei counterstained with TO-PRO-3 (red). Scale bars: B, 25 μ m; C, 5 μ m. The inner segments of photoreceptors (A, green) are crammed with mitochondria that enhance refractive index and convert the inner segments to optical wave guides (reviewed in Sterling, 2003; Hoang et al., 2002). Though this effect was predominantly studied for inner segments of cones in diurnal primates, some data were also obtained for rods of the nocturnal rat (Enoch and Tobey, 1981; Winston, 1981). Additionally, long mitochondria running along the inner segments were demonstrated using TEM in a number of mammalian species for which we show the inverted pattern: ferret (Kageyama and Wong-Riley, 1984), rabbit (Townes-Anderson et al., 1988), mouse (Carter-Dawson and Lavail, 1979). Immunostaining of mitochondria shows an array of densely packed parallel mitochondria spanning the length of the inner segments in the latter species (B, C). Müller glia cells (A, blue) were recently also demonstrated to be optical wave guides transmitting light from the inner margin of the retina to the ONL (Franze et al., 2007). However, in the ONL the processes of Müller cells branch into fine laminar extensions that cannot guide light. Indeed, a notable change of the optical properties of the retina takes place at the ONL border (Franze et al., 2007, fig 2a). Effective transmission of light through the system of microlenses formed by a column of rod nuclei (A, red) with the inverted pattern following from our results would close the gap between Müller cells and inner segments of rod cells and accomplish an effective optical path through the whole retina. Of course, it still has to be understood in more detail how light can be transmitted from Müller cells to the first rod perikarya of columns, and from the last perikarya to the inner segments.

Figure S15.

Scheme summarizing the evolution of opsin genes and nuclear architecture of photoreceptors in vertebrates. For reviews on the evolution of opsins see (Bowmaker and Hunt, 2006; Davies et al., 2007; Trezise and Collin, 2005).



Evolution of rod nuclear architecture in mammals

The inverted pattern is unique to mammals. Comparison of our results and transmission electron microscopic (TEM) images of mouse rods (Carter-Dawson and LaVail, 1979; Helmlinger et al., 2006; see also Supplemental Figure S8) showed that the inverted pattern can also be reliably recognized in TEM images. An intense search in published TEM data confirmed that the inverted pattern occurs only in rod cells of mammals. In particular, rods of other vertebrates always have a conventional pattern, including the rods of owls, specialized nocturnal birds (Braekevelt, 1993; Braekevelt et al., 1996).

Our results leave not doubt that – despite strong conservation of the conventional pattern in the evolution of eukaryotes and, in particular, of multicellular animals – the nuclear architecture of rods was modified several times in the evolution of mammals (main text, Fig 6). This raises the question whether the inverted pattern (1) was developed independently by several nocturnal mammalian groups or (2) originated once and was repeatedly lost by diurnal mammals. To answer this question data on the evolution of mammals and their vision have to be taken into account.

It is generally accepted that the survival of early mammals was facilitated by homeothermy (the ability to maintain a stable body temperature) which allowed them to occupy nocturnal niches during the reign of the predominantly diurnal dinosaurs (see, e.g., Kielan-Jaworowska et al., 2004). Mammals remained predominantly small nocturnal animals until the end of the Mesozoic (ca. 65 mya) when the extinction of dinosaurs allowed their adaptive radiation in other niches. Therefore adaptation to nocturnal vision had to take place early in the evolution of mammals (Ahnelt and Kolb, 2000; Peichl, 2005). Indeed, all recent mammals lost two of the four cone opsin genes serving color vision in birds and reptiles (see Figure). One of them (Rh2) is lacking in both Monotremata and Theria (Marsupialia + Eutheria) which means that it was probably lost before their

separation ca. 200 mya. Each of the two branches in parallel lost one more cone opsin, SWS1 and SWS2, respectively (Bowmaker and Hunt, 2006; Davies et al., 2007; Trezise and Collin, 2005).

To a point, mammals still remain a nocturnal group: more than half of all mammalian species and the vast majority of small mammals are nocturnal. A proportion of recent nocturnal eutherian mammals has also lost the functional SWS1 gene and became cone monochromats. Diurnal niches were independently invaded by dichromatic representatives of different phylogenetic branches of mammals which independently re-adapted to diurnal vision. This process is also confirmed by studies of the molecular evolution of visual pigments. The phylogenetic branch that includes Primates (Euarchonta) contains several nocturnal and diurnal groups. In particular, simiiform primates (monkeys and apes) are diurnal (with the unique exception of the owl monkey *Aotus*), while their closest relatives, tarsiers, are nocturnal and dichromatic. A third cone pigment for color vision (trichromacy) was independently re-acquired three times in different representatives of simiiform primates by different genetic modifications (Bowmaker and Hunt, 2006; Jacobs et al., 1996).

With regard to the organization of the retina, it should first be noted that in both nocturnal marsupials and eutherians one finds specialized nocturnal retinas with a high number of ONL tiers, high photoreceptor densities and a low percentage of cones. Our data and TEM observations (Fleming et al., 1996; Young and Pettigrew, 1991) confirm the inverted pattern in both Australian and South American marsupials; it also develops in a fashion similar to mouse during terminal differentiation of rods. By contrast, the two studied (out of the three recent) monotreme genera, although predominantly nocturnal, have a retina with only 2-3 ONL tiers, a moderate rod density (85,000 -130,000 cells/mm²) and a relatively high cone percentage of, at least, 10-15% (our data; (Young and Pettigrew, 1991). Some neuronal types in the retina of monotremata appear homologous to those of

sauropsid reptiles, but have no obvious counterparts in other mammals (Young and Vaney, 1990). Monotreme rod nuclei have a conventional pattern, even though echidna rod nuclei show some similarity to the inverted one (Young and Pettigrew, 1991). Taken together, these facts imply that the inverted pattern most likely appeared in a common ancestor of the Marsupialia and Eutheria, probably after divergence of the Monotremata and Theria (see Figure).

The conclusion about a monophyletic (rather than multiple) origin of the inverted pattern is supported by the organization of rod nuclei in the nocturnal monkey, *Aotus*. Simiiform primates (diurnal, as mentioned above) are characterized by rods with the conventional pattern. Even a clearly manifested and relatively old adaptation to nocturnal vision – owl monkeys separated from their diurnal relatives ca. 20 myo and lost the SWS1 opsin gene – has not led to an inverted pattern. Optical properties of ONL in *Aotus* are improved in a different fashion, by a central positioning of the relatively large nucleolus in photoreceptor nuclei.

The conventional nuclear architecture was repeatedly re-acquired by therian groups which returned to a diurnal life style. The evolution of the retina and nuclear architecture following a change in life style is illustrated in several cases by mammals with circadian biology different from that of their close relatives. The coati, one of the few diurnal carnivores, shows clear differences from its close nocturnal relatives. The crab-eating raccoon *Procyon cancrivorus* has a pronouncedly nocturnal retina (450 000 rods/mm², 1% cones) with a clear inverted pattern, while the ringtailed coati *Nasua nasua* has only 100 000 rods/mm² and ca. 15% cones. Coati rod nuclei are nearer to the conventional pattern (several large partially interconnected heterochromatin foci). Guinea pigs (*Cavia porcellus*) are crepuscular to diurnal in nature, but retain an intrinsic physiological rhythm similar to that of the nocturnal rat (Kurumiya and Kawamura, 1988). They have ca. 150 000 rods/mm², only 3-4 tiers of photoreceptors and up to

Cell, Volume 137

17% cones, but their rod nuclei retain a clear inverted pattern. Also the Nile rat *Arvicanthis*, one of the few diurnal Murinae (to which belong, e.g., mice and rats), has a retina with only about 6 tiers of photoreceptors and up to 33% cones, but retains the inverted pattern ((Bobu et al., 2006) and images kindly provided by D. Hicks). These two examples suggest that nuclear architecture is the most conservative element in retinal re-adaptation to a diurnal life style. The few species in which an intermediate pattern was observed are diurnal and possibly illustrate the last stage of re-adaptation to diurnal vision.

One could think that re-acquisition of the conventional pattern was achieved simply by accumulation of deleterious mutations affecting concentration of heterochromatin in the central part of the nucleus. However, explanations of this type usually are sufficient only in the case of clearly regressive evolution. Cone photoreceptors are a good example here. Whereas the shortwave sensitive (SWS1) opsin was independently lost in various nocturnal eutherians, the longwave sensitive (LWS) opsin, as far as presently known, is universally retained in mammals (Bowmaker and Hunt, 2006). All mammalian retinæ, even the most nocturnal and the most diurnal ones, possess both rods and cones (reviews: Ahnelt and Kolb, 2000; Peichl, 2005). The reason for such conservation is the complexity of these processes. Differentiation of photoreceptor cells and transcription of genes specific for them are regulated by a complex network of transcription factors (for review see (Hennig et al., 2008), some of which have effects far beyond the rod cell nuclear architecture (Corbo and Cepko, 2005; Helmlinger et al., 2006). Restoration of the conventional pattern therefore should have needed re-adjustment of the regulation network (Davidson and Erwin, 2006) and, respectively, demanded selective pressure for the conventional pattern (see, e.g., (Ridley, 2005)) - note that even such seemingly obvious cases of regressive evolution as reduction of eyes in cave fish can actually be driven by natural selection for some other traits, c.f. Jeffery, 2008). The inference of selective pressure for the conventional pattern in

diurnal mammals is additionally supported by the consideration that from a physical point of view the light-guiding ability of rods with inverted pattern should remain a certain advantage even for diurnal animals because most of them (e.g., humans) have retained moderate night vision.

Table S1. Circadian biology and rod cell nuclear pattern in mammals

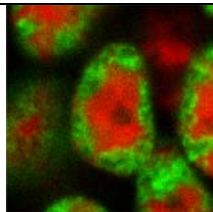
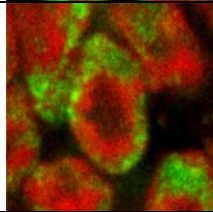
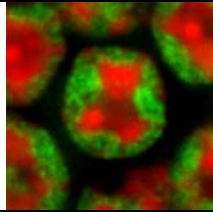
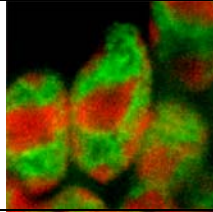
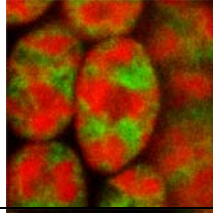
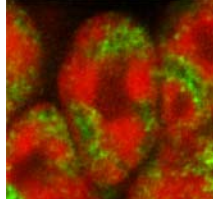
	diurnal	crepuscular	nocturnal
conventional	Wild boar Domestic pig Red squirrel Grey squirrel Chipmunk Woodchuck Tree shrew Crab-eating macaque Human	Grevy's zebra Donkey Domestic horse	
intermediate	Coati (closer to conventional) Mouflon Cow (closer to inverted)		
inverted		Fallow deer Red deer Western roe deer Mongolian gerbil Guinea pig	Sika deer Domestic cat Red fox Arctic fox Ferret Crab-eating raccoon Velvety free-tailed bat Seba's short-tailed bat Pallas' long-tongued bat Spear-nosed bat Domestic mouse Brown rat Chinchilla Flying squirrel Rabbit Colugo (flying lemur) Mouse lemur Hedgehog tenrec Mouse opossum

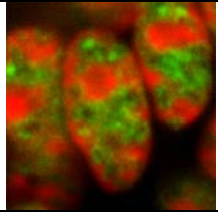
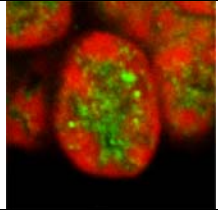
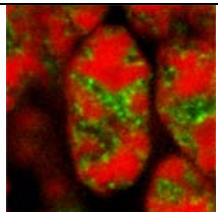
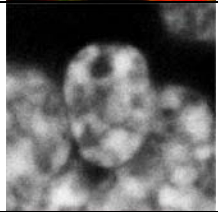
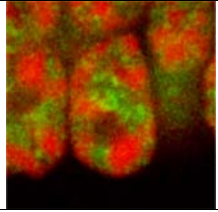
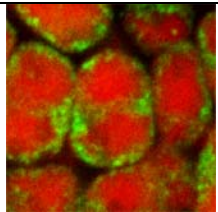
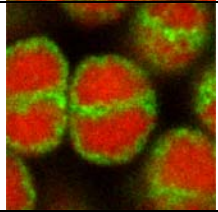
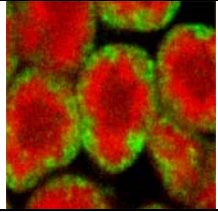
Information for individual species, including characteristic images of rod nuclei, is presented Table S2.

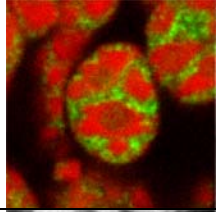
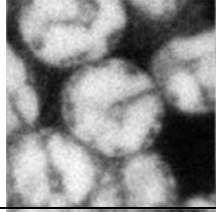

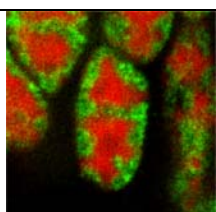
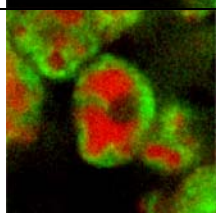
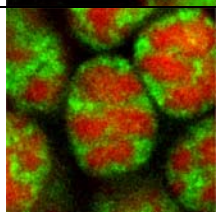
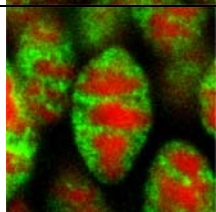
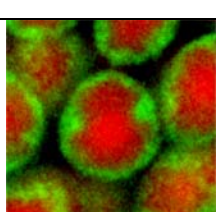
Table S2. Nuclear architecture in rods of the species studied

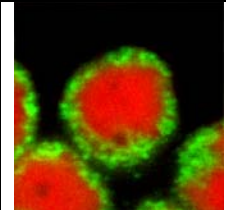
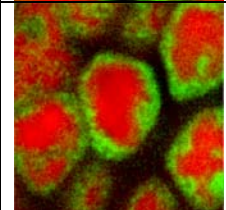
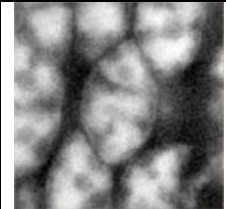
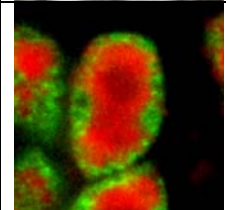
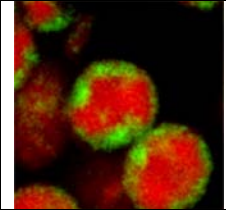
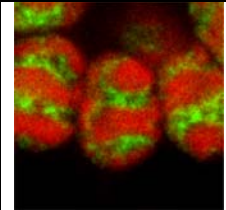
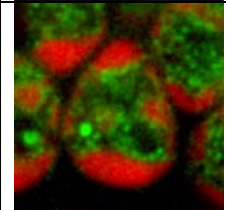
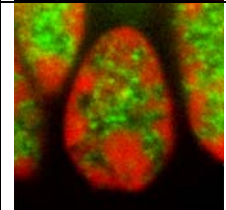
Left column shows the distribution of euchromatin (green, anti-H3K4me3 immunostaining); nuclei were counterstained with DAPI (red); chromocenters in some animals (GC-rich) remain poorly stained with DAPI. The few black and white images show nuclei after DAPI staining only (old material that could not be immunostained).

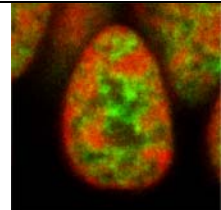
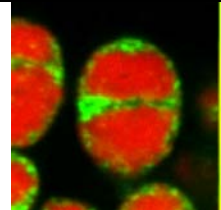
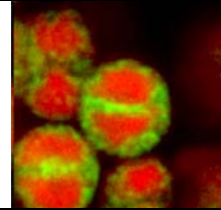
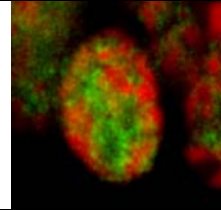
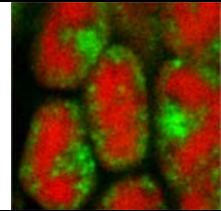
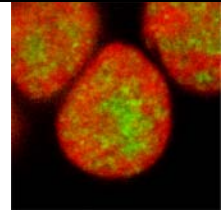
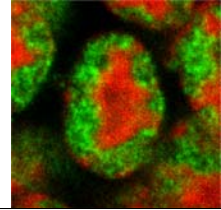
Characteristics of activity patterns were taken from Nowak (1991); where necessary, information from special publications was added.


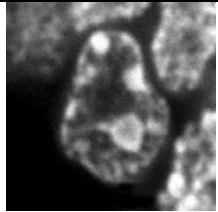
Taxon of interest and accompanying data	
—	<i>scale bar for all images = 5 μm</i>
Cetartiodactyla	
	Fallow deer, <i>Dama dama</i> Crepuscular activity peak, some diurnal and nocturnal activity Hunted animal, some months old. Courtesy E. Noll, MPI for Brain Research
	Sika deer. <i>Cervus nippon</i> Mainly nocturnal , some activity during daylight Hunted animal, young adult. Eye collection of the MPI for Brain Research
	Red deer. <i>Cervus elaphus</i> Crepuscular activity peak, some diurnal and nocturnal activity Hunted animal. Courtesy E. Noll, MPI for Brain Research
	Western roe deer. <i>Capreolus capreolus</i> Crepuscular activity peak, some diurnal and nocturnal activity Hunted animal. Courtesy E. Noll, MPI for Brain Research
	Mouflon, <i>Ovis musimon</i> Mainly diurnal , some nocturnal activity Culled animal, some months old. Courtesy E. Noll, MPI for Brain Research
	Cow, <i>Bos taurus</i> Mainly diurnal , some crepuscular activity Slaughterhouse material

	<p>Wild boar, <i>Sus scrofa</i> Diurnal by nature (nocturnal when habitat is shared with humans) Hunted older male. Courtesy E. Noll, MPI for Brain Research</p>
	<p>Domestic pig, <i>Sus scrofa</i> Diurnal Young adult. Slaughterhouse material.</p>
Perissodactyla	
	<p>Grevy's zebra, <i>Equus grevyi</i> Diurnal and nocturnal activity, peak activity during evening (crepuscular). Culled animal. Courtesy J. Bhattacharjee, Egerton University, Njoro, Kenya</p>
	<p>Donkey, <i>Equus asinus</i> Diurnal and nocturnal activity with morning and late afternoon activity peaks (crepuscular) Adult animal. Slaughterhouse material. Courtesy J. González-Soriano, Universidad Complutense, Madrid, Spain DAPI staining only.</p>
	<p>Domestic horse, <i>Equus caballus</i> Diurnal and nocturnal activity with morning and evening activity peaks (crepuscular) Adult/old animal. Slaughterhouse material</p>
Carnivora	
	<p>Cat, <i>Felis catus</i> Nocturnal and crepuscular Post mortem experimental material. Courtesy U. Eysel, Ruhr-Universität Bochum and K. Schmidt, MPI for Brain Research</p>
	<p>Red fox, <i>Vulpes vulpes</i> Nocturnal and crepuscular Hunted animal, adult. Courtesy E. Noll, MPI for Brain Research</p>
	<p>Arctic fox, <i>Alopex lagopus</i> Active at any time of day according to Nowak 1991, but rather nocturnal (Eberhardt et al. 1981) Young adult. Eye collection of the MPI for Brain Research</p>

	<p>Ferret, <i>Mustela putorius</i> Nocturnal Young animal, post mortem experimental material. Courtesy M. Leinweber, MPI for Neurobiology, Munich</p>
	<p>Crab-eating raccoon, <i>Procyon cancrivorous</i> Mainly nocturnal 7-8 y old, post mortem experimental material. Courtesy B. Pohl, Veterinary University Hannover</p>
	<p>Coati, <i>Nasua nasua</i> Primarily diurnal, adult males also active at night 11 year old female, post mortem experimental material. Courtesy B. Pohl, Veterinary University Hannover</p>
Chiroptera (all studied species belong to the Yangochiroptera)	
	<p>Velvety free-tailed bat, <i>Mollossus mollossus</i> Nocturnal, but foraging flights often start before sunset Adult animal, post mortem experimental material. Courtesy B. Müller, MPI for Brain Research and M. Kössl, University Frankfurt/M.</p>
	<p>Seba's short-tailed bat, <i>Carollia perspicillata</i> Nocturnal Post mortem experimental material. Courtesy B. Müller, MPI for Brain Research and M. Kössl, University Frankfurt/M.</p>
	<p>Pallas' long-tongued bat, <i>Glossophaga soricina</i> Nocturnal Post mortem experimental material. Courtesy B. Müller, MPI for Brain Research and Y. Winter, MPI for Ornithology, Seewiesen</p>
	<p>Spear-nosed bat, <i>Phyllostomus discolor</i> Nocturnal Adult animal, post mortem experimental material. Courtesy B. Grothe, University of Munich</p>
Rodentia Myomorpha	
	<p>Domestic mouse, <i>Mus musculus</i> Mainly nocturnal 9 month old animal (see Material and Methods)</p>

	<p>Brown rat, <i>Rattus norvegicus</i> Nocturnal Adult animal, post mortem experimental material. Courtesy M. Nosov, MPI for Neurobiology, Munich</p>
	<p>Mongolian gerbil, <i>Meriones unguiculatus</i> Nocturnal and diurnal activity, probably crepuscular (Weinert et al. 2007) Age 65 days (P65), post mortem experimental material. Courtesy M.Ford, University of Munich</p>
<p>Rodentia Hystricomorpha</p>	
	<p>Chinchilla, <i>Chinchilla laniger</i> Mostly nocturnal and crepuscular activity, some diurnal activity (predominantly nocturnal according to Ebensperger and Blumstein 2006) Eye collection of the MPI for Brain Research DAPI staining only: clear inverted pattern</p>
	<p>Domestic guinea pig, <i>Cavia porcellus</i> Crepuscular to diurnal Animal house of the MPI for Brain Research Exemplifies transition to diurnal life style (see Supplementary Data 1)</p>
<p>Rodentia Sciuromorpha</p>	
	<p>Flying squirrel, <i>Pteromys volans</i> Strictly nocturnal Wild animal found dead. Courtesy I.K. Hanski, Finnish Museum of Natural History, Helsinki.</p>
	<p>Red squirrel, <i>Sciurus vulgaris</i> Diurnal Eye collection of the MPI for Brain Research,</p>
	<p>Grey squirrel, <i>Sciurus carolinensis</i> Diurnal Culled animal. Courtesy G. Jeffery, University College London, and the Forestry Commission of England</p>
	<p>Chipmunk, <i>Tamias sibiricus</i> Diurnal Eye collection of the MPI for Brain Research</p>

	<p>Woodchuck, <i>Marmota monax</i> Diurnal Post mortem experimental material. Courtesy P. Dammann, Central Animal Laboratory, Essen University Medical School</p>
<p>Lagomorpha</p>	
	<p>Rabbit, <i>Oryctolagus cuniculus</i> Nocturnal, some crepuscular activity Post mortem experimental material. Courtesy Dr. Thein, University of Munich</p>
<p>Dermoptera, Scadentia, and Primates</p>	
	<p>Colugo (flying lemur), <i>Galeopterus variegatus</i> Nocturnal Wild male adult found dead. Courtesy N. Lim, National University of Singapore and Raffles Museum of Biodiversity Research, Singapore</p>
	<p>Tree shrew, <i>Tupaia belangeri</i> Diurnal Adult animal, post mortem experimental material from breeding colony at the MPI for Brain Research</p>
	<p>Mouse lemur, <i>Microcebus myoxinus</i> Nocturnal Adult animal, post mortem experimental material from breeding colony. Courtesy A. Kaiser, Veterinary University Hannover</p>
	<p>Crab-eating macaque, <i>Macaca fascicularis</i> Diurnal Old female, post mortem experimental material from breeding colony. Courtesy M. Munk, MPI for Brain Research</p>
<p>Afrotheria</p>	
	<p>Hedgehog tenrec, <i>Echinops telfairi</i> Nocturnal Post mortem experimental material from breeding colony. Courtesy H. Künzle, Ludwig Maximilians University Munich</p>
<p>Marsupialia</p>	

	Mouse opossum, <i>Thylamys elegans</i> Nocturnal Post mortem experimental material. Courtesy A. Palacios, Universidad de Valparaiso, Chile
Monotremata	
	Platypus, <i>Ornithorhynchus anatinus</i> Crepuscular / Predominantly nocturnal (Grant and Temple-Smith 1998) Post mortem experimental material. Courtesy J.D. Pettigrew & P.R. Manger, University of Queensland, Australia. Likely primary absence of the inverted pattern (see Supplementary Data 1)

SUPPLEMENTAL REFERENCES

Albiez, H., Cremer, M., Tiberi, C., Vecchio, L., Schermelleh, L., Dittrich, S., Küpper, K., Joffe, B., Thormeyer, T., von Hase, J., Yang, S., Rohr, K., Leonhardt, H., Solovei, I., Cremer, C., Fakan, S., Cremer, T. Chromatin domains and the interchromatin compartment form structurally defined and functionally interacting nuclear networks. *Chromosome Res* 14, 707-33.

Barer, R. J. S. (1954). Refractometry of living cells, part I. Basic principles. *Q J Microsc Sci* 95, 399-423.

Bobu, C., Craft, C. M., Masson-Pevet, M., and Hicks, D. (2006). Photoreceptor organization and rhythmic phagocytosis in the Nile rat *Arvicanthis ansorgei*: a novel diurnal rodent model for the study of cone pathophysiology. *Invest Ophthalmol Vis Sci* 47, 3109-3118.

Bowmaker, J. K., and Hunt, D. M. (2006). Evolution of vertebrate visual pigments. *Curr Biol* 16, R484-489.

Braekevelt, C. R. (1993). Fine structure of the retinal photoreceptors of the great horned owl (*Bubo virginianus*). *Histol Histopathol* 8, 25-34.

Braekevelt, C. R., Smith, S. A., and Smith, B. J. (1996). Fine structure of the retinal photoreceptors of the barred owl (*Strix varia*). *Histol Histopathol* 11, 79-88.

Brunsting, A., and Mullaney, P. F. (1974). Differential light scattering from spherical mammalian cells. *Biophys J* 14, 439-453.

Cremer, M., von Hase, J., Volm, T., Brero, A., Kreth, G., Walter, J., Fischer, C., Solovei, I., Cremer, C., Cremer, T. (2001). Non-random radial higher-order chromatin arrangements in nuclei of diploid human cells. *Chromosome Res* 9, 541-67.

Davidson, E. H., and Erwin, D. H. (2006). Gene regulatory networks and the evolution of animal body plans. *Science* 311, 796-800.

Davies, W. L., Carvalho, L. S., Cowing, J. A., Beazley, L. D., Hunt, D. M., and Arrese, C. A. (2007). Visual pigments of the platypus: a novel route to mammalian colour vision. *Curr Biol* 17, R161-163.

Djaldetti, M., Bessler, H., and Rifkind, R. A. (1972). Hematopoiesis in the embryonic mouse spleen: an electron microscopic study. *Blood* 39, 826-841.

Dkhissi-Benyahya, O., Szel, A., Degrip, W. J., and Cooper, H. M. (2001). Short and mid-wavelength cone distribution in a nocturnal Strepsirrhine primate (*Microcebus murinus*). *J Comp Neurol* 438, 490-504.

Drezek, R., Dunn, A., and Richards-Kortum, R. (1999). Light scattering from cells: finite-difference time-domain simulations and goniometric measurements. *Appl Opt* 38, 3651-3661.

Drezek, R., Guillaud, M., Collier, T., Boiko, I., Malpica, A., Macaulay, C., Follen, M., and Richards-Kortum, R. (2003). Light scattering from cervical cells throughout neoplastic progression: influence of nuclear morphology, DNA content, and chromatin texture. *J Biomed Opt* 8, 7-16.

Ebensperger, L. A., and Blumstein, D. T. (2006). Sociality in New World hystricognath rodents is linked to predators and burrow digging. *Behav Ecol* 17, 410-418.

Eberhardt, L. E., Hanson, W. C., Bengtson, J. L., Garrott, R. A., and Hanson, E. E. (1982). Arctic Fox Home Range Characteristics in an Oil-Development Area. *J Wildlife Management* 46, 183-190.

Enoch, J. M., and Tobey, F. L. (1981). Waveguide properties of retinal receptors: techniques and observations, In *Vertebrate photoreceptor optics* (Berlin: Springer), pp. 169-218.

Fleming, P. A., Braekevelt, C. R., Harman, A. M., and Beazley, L. D. (1996). Retinal pigment epithelium and photoreceptor maturation in a wallaby, the quokka. *J Comp Neurol* 370, 47-60.

Gerke, C. G., Hao, Y., and Wong, F. (1995). Topography of rods and cones in the retina of the domestic pig. *Hong Kong Med J* 1, 302-308.

Hallett, P. E. (1987). The scale of the visual pathways of mouse and rat. *Biol Cybern* 57, 275-286.

Henegariu, O., Bray-Ward, P., and Ward, D. C. (2000). Custom fluorescent-nucleotide synthesis as an alternative method for nucleic acid labeling. *Nat Biotechnol* 18, 345-348.

Hennig, A. K., Peng, G. H., and Chen, S. (2008). Regulation of photoreceptor gene expression by Crx-associated transcription factor network. *Brain Res* 1192, 114-133.

Hoang, Q. V., Linsenmeier, R. A., Chung, C. K., and Curcio, C. A. (2002). Photoreceptor inner segments in monkey and human retina: mitochondrial density, optics, and regional variation. *Vis Neurosci* 19, 395-407.

Ijdo, J. W., Wells, R. A., Baldini, A., and Reeders, S. T. (1991). Improved telomere detection using a telomere repeat probe (TTAGGG)_n generated by PCR. *Nucleic Acids Res* 19, 4780.

Jacobs, G. H., Neitz, M., Deegan, J. F., and Neitz, J. (1996). Trichromatic colour vision in New World monkeys. *Nature* 382, 156-158.

Cell, Volume 137

Jeffery, G., Darling, K., and Whitmore, A. (1994). Melanin and the regulation of mammalian photoreceptor topography. *Eur J Neurosci* 6, 657-667.

Jeffery W.R. (2008) Emerging model systems in evo-devo: cavefish and microevolution of Development. *Evol and Development* 10, 265-272.

Jeon, C. J., Strettoi, E., and Masland, R. H. (1998). The major cell populations of the mouse retina. *J Neurosci* 18, 8936-8946.

Kageyama, G. H., and Wong-Riley, M. T. (1984). The histochemical localization of cytochrome oxidase in the retina and lateral geniculate nucleus of the ferret, cat, and monkey, with particular reference to retinal mosaics and ON/OFF-center visual channels. *J Neurosci* 4, 2445-2459.

Kielan-Jaworowska, Z., Cifelli, R. L., and Luo, Z.-X. (2004). *Mammals from the Age of Dinosaurs: Origins, Evolution, and Structure* (New York: Columbia University Press).

Kipling, D., and Cooke, H. J. (1990). Hypervariable ultra-long telomeres in mice. *Nature* 347, 400-402.

Krebs, W., and Friedrich, I. (1982). Quantitative morphology of bovine retina, In *The Structure of the Eye*, J. G. Hollyfield, ed. (New York: Elsevier), pp. 175-182.

Kurumiya, S., and Kawamura, H. (1988). Circadian oscillation of the multiple unit activity in the guinea pig suprachiasmatic nucleus. *J Comp Physiol [A]* 162, 301-308.

Lyubarsky, A. L., Falsini, B., Pennesi, M. E., Valentini, P., and Pugh, E. N., Jr. (1999). UV- and midwave-sensitive cone-driven retinal responses of the mouse: a possible phenotype for coexpression of cone photopigments. *J Neurosci* 19, 442-455.

Nowak, R. M. (1991). *Walker's Mammals of the World*, 5-th edition (Baltimore & London: Johns Hopkins University Press).

Peichl, L., Kunzle, H., and Vogel, P. (2000). Photoreceptor types and distributions in the retinae of insectivores. *Vis Neurosci* 17, 937-948.

Pietras, D. F., Bennett, K. L., Siracusa, L. D., Woodworth-Gutai, M., Chapman, V. M., Gross, K. W., Kane-Haas, C., and Hastie, N. D. (1983). Construction of a small *Mus musculus* repetitive DNA library: identification of a new satellite sequence in *Mus musculus*. *Nucleic Acids Res* 11, 6965-6983.

Ridley, M., ed. (2005). *Evolution* (Blackwell).

Schotta, G., Lachner, M., Sarma, K., Ebert, A., Sengupta, R., Reuter, G., Reinberg, D., and Jenuwein, T. (2004). A silencing pathway to induce H3-K9 and H4-K20 trimethylation at constitutive heterochromatin. *Genes Dev* 18, 1251-1262.

Steinberg, R. H., Reid, M., and Lacy, P. L. (1973). The distribution of rods and cones in the retina of the cat (*Felis domesticus*). *J Comp Neurol* 148, 229-248.

Szel, A., and Rohlich, P. (1992). Two cone types of rat retina detected by anti-visual pigment antibodies. *Exp Eye Res* 55, 47-52.

Townes-Anderson, E., Dacheux, R. F., and Raviola, E. (1988). Rod photoreceptors dissociated from the adult rabbit retina. *J Neurosci* 8, 320-331.

Trezise, A. E., and Collin, S. P. (2005). Opsins: evolution in waiting. *Curr Biol* 15, R794-796.
Wikler, K. C., Williams, R. W., and Rakic, P. (1990). Photoreceptor mosaic: number and distribution of rods and cones in the rhesus monkey retina. *J Comp Neurol* 297, 499-508.

Walter, J., Joffe, B., Bolzer, A., Albiez, H., Benedetti, P. A., Müller, S., Speicher, M.R., Cremer, T., Cremer, M., Solovei, I. (2006). Towards many colors in FISH on 3D-preserved interphase nuclei. *Cytogenet Genome Res* 114, 367-378.

Weinert, D., Weinandy, R., and Gattermann, R. (2007). Photic and non-photic effects on the daily activity pattern of Mongolian gerbils. *Physiol Behav* 90, 325-333.

Will, C. L., Urlaub, H., Achsel, T., Gentzel, M., Wilm, M., and Luhrmann, R. (2002). Characterization of novel SF3b and 17S U2 snRNP proteins, including a human Prp5p homologue and an SF3b DEAD-box protein. *Embo J* 21, 4978-4988.

Winston, R. (1981). The visual receptor as light collector, In *Vertebrate photoreceptor optics* (Berlin: Springer), pp. 325-336.

Yamashita, S. (2007). Heat-induced antigen retrieval: mechanisms and application to histochemistry. *Prog Histochem Cytochem* 41, 141-200.

Young, H. M., and Pettigrew, J. D. (1991). Cone photoreceptors lacking oil droplets in the retina of the echidna, *Tachyglossus aculeatus* (Monotremata). *Vis Neurosci* 6, 409-420.

Young, H. M., and Vaney, D. I. (1990). The retinae of Prototherian mammals possess neuronal types that are characteristic of non-mammalian retinae. *Vis Neurosci* 5, 61-66.